Evaluation of the Spline Reconstruction Technique for PET

George A. Kastis* and Dimitra Kyriakopoulou

Research Center of Mathematics, Academy of Athens,

Soranou Efessiou 4, Athens 11527, Greece

Anastasios Gaitanis

Biomedical Research Foundation of the Academy of Athens (BRFAA),

Soranou Efessiou 4, Athens 11527, Greece

Yolanda Fernández

Centre d'Imatge Molecular Experimental (CIME), CETIR-ERESA, Barcelona, Spain

Brian F. Hutton

Institute of Nuclear Medicine, University College London, London, UK†

Athanasios S. Fokas

Department of Applied Mathematics and Theoretical Physics,

University of Cambridge, Cambridge, CB30WA, UK‡

(Dated: January 29, 2014)

Abstract

Purpose: The Spline Reconstruction Technique (SRT), based on the analytic formula for the inverse Radon transform, has been presented earlier in the literature. In this study, we present an improved formulation and numerical implementation of this algorithm and evaluate it in comparison to FBP.

Methods: The SRT is based on the numerical evaluation of the Hilbert transform of the sinogram via an approximation in terms of 'custom made' cubic splines. By restricting reconstruction only within object pixels and by utilizing certain mathematical symmetries, we achieve a reconstruction time comparable to that of FBP. We have implemented SRT in STIR and have evaluated this technique using simulated data from a clinical PET system, as well as real data obtained from clinical and preclinical PET scanners. For the simulation studies, we have simulated sinograms of a point-source and three digital phantoms. Using these sinograms, we have created realizations of Poisson noise at five noise levels. In addition to visual comparisons of the reconstructed images, we have determined contrast and bias for different regions of the phantoms as a function of noise level. For the real-data studies, sinograms of an ^{18}F-FDG injected mouse, a NEMA NU 4-2008 image quality phantom, and a Derenzo phantom have been acquired from a commercial PET system. We have determined: a) coefficient of variations (COV) and contrast from the NEMA phantom, b) contrast for the various sections of the Derenzo phantom, and c) line profiles for the Derenzo phantom. Furthermore, we have acquired sinograms from a whole-body PET scan of an ^{18}F-FDG injected cancer patient, using the GE Discovery ST PET/CT system. SRT and FBP reconstructions of the thorax have been visually evaluated.

Results: Our results indicate an improvement in FWHM and FWTM in both simulated and real point-source studies. In all simulated phantoms, the SRT exhibits higher contrast and lower bias than FBP at all noise levels, by increasing the COV in the reconstructed images. Finally, in real studies, whereas the contrast of the cold chambers are similar for both algorithms, the SRT reconstructed images of the NEMA phantom exhibit slightly higher COV values than those of FBP. In the Derenzo phantom, SRT resolves the 2-mm separated holes slightly better that FBP. The small-animal and human reconstructions via SRT exhibit slightly higher resolution and contrast than the FBP reconstructions.

Conclusions: The SRT provides images of higher resolution, higher contrast and lower bias than FBP, by increasing slightly the noise in the reconstructed images. Furthermore, it eliminates streak

artifacts outside the object boundary. Unlike other analytic algorithms, the reconstruction time of SRT is comparable with that of FBP. The source code for SRT will become available in a future release of STIR.

Keywords: Image reconstruction-analytical methods, Spline reconstruction, SRT, PET, FBP

I. INTRODUCTION

Positron emission tomography (PET) imaging is an important, noninvasive, nuclear medicine modality that measures the *in vivo* distribution of imaging agents labeled with positron-emitting radionuclides[1]. The importance of PET in detecting, staging and monitoring the progress of several diseases has been established in a plethora of rigorous clinical studies[2]. In oncologic imaging, PET/CT with ^{18}F-FDG plays a crucial role for staging, restaging, and treatment monitoring for cancer patients[3–5]. Furthermore, small-animal PET is becoming an essential imaging modality for preclinical research[1,6,7], as well as for drug development and discovery[8]. It allows each animal to serve as its own control through a series of longitudinal studies, thus eliminating the intersubject variability and also reducing the number of animals required for an experiment.

Image reconstruction is an essential component in tomographic medical imaging, including PET, SPECT (Single-Photon Emission Computed Tomography) and CT (Computed Tomography), allowing a tomographic image to be obtained from a set of two-dimensional projections. In contrast to CT and SPECT which involve the acquisition of projection images, in PET the relevant raw data consist of a list of 'coincidence events' which are created along certain 'lines-of-responses' (LORs). However, coincidence events *can* be grouped into sinograms. The existing image reconstruction methods can be classified into two main categories: (a) analytic methods and (b) iterative (or algebraic) methods. There exist several references on these methods either in books[9–11] or journal articles[12,13].

Filtered backprojection (FBP) is the predominant analytic reconstruction method; mathematically it is based on the inversion of the Radon transform[14–16] through the central slice theorem[17]. The main advantages of FBP are speed and simplicity. FBP assumes a simple Radon model where the data consist of line integrals along the radioactivity distribution, ignoring the randomness of the gamma-ray counting process. However, in FBP it is difficult to incorporate complex physical phenomena such as attenuation and scatter. Noise issues are treated by selecting appropriate filtering parameters, such as the roll-off and cutoff frequencies of the reconstruction filter (usually at the expense of spatial resolution). Another disadvantage of FBP is the streak artifacts that are particular prominent near hot regions of the object.

The predominant iterative algorithms are the Maximum Likelihood Expectation Maxi-

mization (MLEM) algorithm[18] and its accelerated successor the Ordered Subsets Expectation Maximization (OSEM) algorithm[19]. The main advantage of the iterative algorithms is the ability to model several aspects of the imaging system, including elements of the noise characteristics, sinogram blurring due to detector crystal penetration, depth of interaction, photon scatter and attenuation in the body[20,21]. As a consequence, iterative methods can improve image quality and achieve considerable resolution recovery. However, iterative algorithms require more computing time and power, particularly when details of the physical model are included.

Iterative techniques are now in widespread use in clinical and preclinical systems. This is due to the recent computer hardware improvements (processing and storage) and the speed improvement provide by OSEM. Most commercial clinical and preclinical PET systems allow the use of either FBP or OSEM for image reconstruction. Currently, in OSEM the main challenge is the selection of the proper number of subsets and iterations[22], as well as the choice of a suitable post-reconstruction filter (if needed). Stopping the algorithm at the proper number of iterations is important, since EM-based algorithms suffer from noise/bias trade-off. Stopping the iteration process after convergence is reached results in a noisy image, whereas stopping the process too soon results in a less noisy image, which however is biased towards the image assumed at the initial step. In order to resolve this issue, several regularisation schemes have been proposed[23]. In spite of these improvements, a recent dynamic brain PET study by Reilhac *et al.*[24] concludes that analytical methods are more robust to low count data than iterative methods. Furthermore, the positivity constraint imposed to the sinogram and image space by the EM-based reconstruction algorithms, leads to overestimation (positive bias) of the low activity regions[24–26].

In a recent study by Conti *et al.*[27] it was demonstrated that TOF FBP has improved performance over TOF OSEM. In particular, it was shown that the TOF gain in TOF FBP can be used as a sensitivity amplifier, reducing the number of counts necessary to produce an image of the same characteristics. On the other hand, it was observed that there were some limitations in the TOF gain of TOF OSEM, especially at low count cases. TOF can be applied to SRT in a manner similar to FBP. Specifically, TOF can be applied by confidence weighting each projection during backprojection for each TOF bin[27].

In this study, we present an improved numerical implementation of an analytic, two-dimensional, reconstruction technique called SRT (Spline Reconstruction Technique). Fur-

thermore, we evaluate this new technique in comparison to FBP, using simulated data from a clinical PET system, as well as real data obtained from clinical and preclinical PET scanners. For this evaluation we employ the Open Source software library called STIR (Software for Tomographic Image Reconstruction)[28].

The SRT algorithm is based on an analytic formula for the inverse Radon transform presented earlier in the literature[29,30]. Here, we present an improved formulation of the numerical implementation which corrects certain singularity issues of the earlier version. SRT involves the numerical evaluation of the Hilbert transform of the sinogram via an approximation in terms of 'custom made' cubic splines. The use of splines for computing the inverse Radon transform is not new; in particular see La Rivière and Pan[31] and Horbelt *et al.*[32]. Furthermore, by employing sinogram thresholding, we restrict reconstruction only within object pixels, thus eliminating the streak artifacts outside the object and hence reconstructing a 'cleaner' image. In addition, by exploiting certain mathematical symmetries, we are able to improve the reconstruction time to a level comparable with FBP.

II. MATERIALS AND METHODS

A. Spline Reconstruction Technique (SRT)

Consider a line L specified by two real numbers ρ and θ, where $-\infty < \rho < \infty$ and $0 \leq \theta < 2\pi$. For a given θ, a point on this line in Cartesian coordinates (x_1, x_2), can be expressed in terms of the *local coordinates* (ρ, τ) by the equations

$$x_1 = \tau \cos\theta - \rho \sin\theta \text{ and } x_2 = \tau \sin\theta + \rho \cos\theta, \tag{1}$$

where τ is a parameter along L.

The line integral of a function $f(x_1, x_2)$ along the line L is called its *Radon transform*, and is denoted by $\widehat{f}$[14,15]:

$$\widehat{f}(\rho,\theta) = \int_{-\infty}^{\infty}\int_{-\infty}^{\infty} f(x_1,x_2)\,\delta(\rho - x_2\cos\theta + x_1\sin\theta)\,dx_1dx_2, \quad -\infty < \rho < \infty, \quad 0 \leq \theta < 2\pi, \tag{2}$$

where $\delta(\cdot)$ the *Dirac* delta function. In the rotated coordinate system (ρ, τ), where

$$\rho = x_2 \cos\theta - x_1 \sin\theta \text{ and } \tau = x_2 \sin\theta + x_1 \cos\theta, \tag{3}$$

the *Radon transform* can be expressed as

$$\widehat{f}(\rho,\theta)=\int_{-\infty}^{\infty} f\left(\tau\cos\theta-\rho\sin\theta,\tau\sin\theta+\rho\cos\theta\right)d\tau, \qquad -\infty<\rho<\infty,\ \ 0\le\theta<2\pi. \tag{4}$$

85 In medical applications the above integral has finite support.

Associated with Eq. (4) there exists the following inverse problem: Given $\widehat{f}(\rho,\theta)$ for all $0\le\theta<2\pi$ and $-\infty<\rho<\infty$, determine the corresponding function $f(x_1,x_2)$. The relevant formula, called the *Inverse Radon transform*[14,15], can be expressed in the following form[33]:

$$f(x_1,x_2)=\frac{1}{2i\pi}\left(\frac{\partial}{\partial x_1}-i\frac{\partial}{\partial x_2}\right)\int_0^{2\pi} e^{i\theta}F(\rho,\theta)\Big|_{\rho=x_2\cos\theta-x_1\sin\theta} d\theta, \tag{5}$$

where $F(\rho,\theta)$ denotes half the Hilbert transform of $\widehat{f}(\rho,\theta)$ with respect to ρ, *i.e.*

$$F(\rho,\theta)\equiv\frac{1}{2\pi}\oint_{-\infty}^{\infty}\frac{\widehat{f}(r,\theta)}{r-\rho}dr, \qquad -\infty<\rho<\infty, \qquad 0\le\theta<2\pi \tag{6}$$

and $\oint$ denotes the principal value integral.

Eq. (5) can be written in the form

$$f(x_1,x_2)=-\frac{1}{2\pi}\int_0^{2\pi}\left[\frac{\partial F(\rho,\theta)}{\partial\rho}\right]_{\rho=x_2\cos\theta-x_1\sin\theta} d\theta, \qquad -\infty<x_1,x_2<\infty. \tag{7}$$

Indeed, inserting the operator $\left(\frac{\partial}{\partial x_1}-i\frac{\partial}{\partial x_2}\right)$ inside the integral in the right hand side of Eq. (5), we find

$$\left(\frac{\partial}{\partial x_1}-i\frac{\partial}{\partial x_2}\right)F(x_2\cos\theta-x_1\sin\theta,\theta)=-\left(\sin\theta+i\cos\theta\right)\frac{\partial F(\rho,\theta)}{\partial\rho}, \tag{8}$$

where ρ is defined in Eq. (3). Using Eq. (8), Eq. (5) becomes Eq. (7).

For the numerical calculation of the Hilbert transform of $\widehat{f}(\rho,\theta)$ we assume that $\widehat{f}(\rho,\theta)$ has support in the interval $-1\le\rho\le1$ with $\widehat{f}(-1,\theta)=\widehat{f}(1,\theta)=0$, and that $\widehat{f}(\rho,\theta)$ is given for every θ at the n points $\{\rho_i\}_1^n$. We denote the value of $\widehat{f}$ at ρ_i by $\widehat{f}_i$, *i.e.*

$$\widehat{f}_i=\widehat{f}(\rho_i,\theta), \qquad \rho_i\in[-1,1], \qquad 0\le\theta<2\pi, \quad i=1,\ldots,n. \tag{9}$$

In the interval $\rho_i\le\rho\le\rho_{i+1}$, we approximate $\widehat{f}(\rho,\theta)$ by cubic splines:

$$\widehat{f}(\rho,\theta)=a_i(\theta)+b_i(\theta)\rho+c_i(\theta)\rho^2+d_i(\theta)\rho^3, \ \ \rho_i\le\rho\le\rho_{i+1}, \ \ 0\le\theta<2\pi, \quad i=1,\ldots,n, \tag{10}$$

with $\{a_i(\theta), b_i(\theta), c_i(\theta), d_i(\theta)\}_1^n$ given by the following expressions:

$$a_i(\theta) = \frac{\rho_{i+1}\widehat{f}_i - \rho_i\widehat{f}_{i+1}}{\Delta_i} + \frac{\widehat{f}_i''}{6}\left(-\rho_{i+1}\Delta_i + \frac{\rho_{i+1}^3}{\Delta_i}\right) + \frac{\widehat{f}_{i+1}''}{6}\left(\rho_i\Delta_i - \frac{\rho_i^3}{\Delta_i}\right), \tag{11a}$$

$$b_i(\theta) = \frac{\widehat{f}_{i+1} - \widehat{f}_i}{\Delta_i} - \frac{\widehat{f}_i''}{6}\left(-\Delta_i + \frac{3\rho_{i+1}^2}{\Delta_i}\right) + \frac{\widehat{f}_{i+1}''}{6}\left(-\Delta_i + \frac{3\rho_i^2}{\Delta_i}\right), \tag{11b}$$

$$c_i(\theta) = \frac{1}{2\Delta_i}(\rho_{i+1}\widehat{f}_i'' - \rho_i\widehat{f}_{i+1}''), \tag{11c}$$

$$d_i(\theta) = \frac{\widehat{f}_{i+1}'' - \widehat{f}_i''}{6\Delta_i}, \tag{11d}$$

where,

$$\Delta_i = \rho_{i+1} - \rho_i \tag{12}$$

and $\widehat{f}_i''$ denotes the second derivative of $\widehat{f}(\rho,\theta)$ with respect to ρ evaluated at ρ_i, *i.e.*

$$\widehat{f}_i'' = \left.\frac{\partial^2\widehat{f}(\rho,\theta)}{\partial\rho^2}\right|_{\rho=\rho_i}, \quad i = 1,\ldots,n. \tag{13}$$

We next show that the function $\partial F/\partial\rho$, where F is defined in Eq. (6), can be approximated as follows:

$$\frac{\partial F(\rho,\theta)}{\partial\rho} = \frac{1}{2\pi}\left\{C(\theta) + \frac{1}{2}(\widehat{f}_n'' - \widehat{f}_1'')\rho + D_{n-1}(\rho,\theta)\ln|\rho-\rho_n| - D_1(\rho,\theta)\ln|\rho-\rho_1| + \sum_{i=1}^{n-2}[D_i(\rho,\theta) - D_{i+1}(\rho,\theta)]\ln|\rho-\rho_{i+1}|\right\}, \quad -1 \le \rho \le 1, \quad 0 \le \theta < 2\pi, \tag{14}$$

where $C(\theta)$ and $\{D_i(\rho,\theta)\}_1^{n-1}$ are defined by the equations

$$C(\theta) = \sum_{i=1}^{n-1}[2c_i(\theta)\Delta_i + \frac{3}{2}d_i(\theta)(\rho_{i+1}^2 - \rho_i^2)], \tag{15a}$$

$$D_i(\rho,\theta) = b_i(\theta) + 2c_i(\theta)\rho + 3d_i(\theta)\rho^2, \quad \rho_i \le \rho \le \rho_{i+1}, \quad i = 1,\ldots,n. \tag{15b}$$

The functions $\{b_i(\theta), c_i(\theta), d_i(\theta)\}_1^n$ appearing in Eq. (15a) and Eq. (15b) are defined by Eqs. (11b)-(11d) via $\{\widehat{f}_i$ and $\widehat{f}_i''\}_1^n$; the functions $\{\widehat{f}_i''(\theta)\}_1^n$ can be computed in terms of $\widehat{f}_i(\theta)$ by solving the following n linear equations:

$$D_i(\rho_{i+1},\theta) = D_{i+1}(\rho_{i+1},\theta), \quad i = 1,\ldots,n-2, \quad 0 \le \theta < 2\pi, \tag{16a}$$

$$D_1(\rho_1,\theta) = D_{n-1}(\rho_n,\theta) = 0. \tag{16b}$$

Before deriving Eq. (14)-(16b), we note that the points $\{\rho_{i+1}\}_{i=1}^{n-1}$ are *removable* logarithmic singularities. This is a direct consequence of Eqs. (16a).

In order to derive Eq. (14) we first note that for the arbitrary function $\widehat{f}(r,\theta)$ the following expression holds:

$$\frac{\partial}{\partial\rho}\oint_{\rho_i}^{\rho_{i+1}}\frac{\widehat{f}(r,\theta)}{r-\rho}dr=\frac{\widehat{f}_{i+1}}{\rho-\rho_{i+1}}-\frac{\widehat{f}_i}{\rho-\rho_i}+\oint_{\rho_i}^{\rho_{i+1}}\frac{\frac{\partial\widehat{f}(r,\theta)}{\partial r}}{r-\rho}dr,\ \ -1\leq\rho\leq 1. \tag{17}$$

Hence,

$$\frac{\partial}{\partial\rho}\oint_{-1}^{1}\frac{\widehat{f}(r,\theta)}{r-\rho}dr=\sum_{i=1}^{n-1}\oint_{\rho_i}^{\rho_{i+1}}\frac{\frac{\partial\widehat{f}(r,\theta)}{\partial r}}{r-\rho}dr. \tag{18}$$

Then, employing the identities

$$\oint_{\rho_i}^{\rho_{i+1}}\frac{dr}{r-\rho} = I_i(\rho), \tag{19a}$$

$$\oint_{\rho_i}^{\rho_{i+1}}\frac{rdr}{r-\rho} = \Delta_i+\rho I_i(\rho), \tag{19b}$$

$$\oint_{\rho_i}^{\rho_{i+1}}\frac{r^2dr}{r-\rho} = \frac{1}{2}(\rho_{i+1}^2-\rho_i^2)+\rho\Delta_i+\rho^2 I_i(\rho), \tag{19c}$$

where

$$I_i(\rho)=\ln\left|\frac{\rho_{i+1}-\rho}{\rho_i-\rho}\right|, \tag{20}$$

Eq. (18) becomes

$$\frac{\partial}{\partial\rho}\oint_{-1}^{1}\frac{\widehat{f}(r,\theta)}{r-\rho}dr = \sum_{i=1}^{n-1}[2c_i\Delta_i+\ \frac{3}{2}d_i(\rho_{i+1}^2-\rho_i^2)]+3\left(\sum_{i=1}^{n-1}d_i\Delta_i\right)\rho+\sum_{i=1}^{n-1}D_i(\rho)\ln\left|\frac{\rho_{i+1}-\rho}{\rho_i-\rho}\right|. \tag{21}$$

Evaluating $\widehat{f}$ as well as the second derivative of $\widehat{f}$ with respect to ρ at $\rho=\rho_i$ and $\rho=\rho_{i+1}$ we obtain four equations relating $\{a_i,b_i,c_i,d_i\}$ with $\left\{\widehat{f}_i,\widehat{f}_{i+1},\widehat{f}_i'',\widehat{f}_{i+1}''\right\}$. These equations imply equations (14). Then, the first two sums in the right-hand-side (RHS) of Eq. (21) yield the first two terms in the RHS of Eq. (14). Similarly, the third sum in the RHS of Eq. (14) yields the following terms:

$$D_{n-1}(\rho,\theta)\ln|\rho-\rho_n|-D_1(\rho,\theta)\ln|\rho-\rho_1|+\sum_{i=1}^{n-2}[D_i(\rho,\theta)-D_{i+1}(\rho,\theta)]\ln|\rho-\rho_{i+1}|. \tag{22}$$

and hence we obtain Eq. (14). Eqs. (16b) imply that there do not exist logarithmic singularities at the $\rho=\rho_n=\rho_1$.

Therefore, the *Inverse Radon transform* of a function $\widehat{f}(\rho,\theta)$, using the splines defined by Eqs. (11a)-(11d), Eq. (12) and Eqs. (15a)-(15b) can be written in the form

$$f(x_1,x_2) = -\frac{1}{4\pi^2}\int_0^{2\pi}\left\{C(\theta)+\frac{1}{2}(\widehat{f}_n''-\widehat{f}_1'')\rho + D_{n-1}(\rho,\theta)\ln|\rho-\rho_n| - D_1(\rho,\theta)\ln|\rho-\rho_1| + \sum_{i=1}^{n-2}[D_i(\rho,\theta)-D_{i+1}(\rho,\theta)]\ln|\rho-\rho_{i+1}|\right\}d\theta, \tag{23}$$

where $C(\theta)$ and $D_i(\rho,\theta)$ are given by Eq. (15a) and Eq. (15b).

We note that in the construction of the so-called 'natural' splines, one requires continuity of the first derivative (the set of equations in (16a)), as well as the conditions $\widehat{f}_1''=\widehat{f}_n''=0$. The former requirement implies that there *cannot* be logarithmic singularities at the interior points $\rho=\rho_i, \quad i=2,\ldots,n-1$. In order to eliminate the logarithmic singularities at the end points $\rho_1=-1$ and $\rho_n=1$, we impose the set of equations in (16b) (instead of $\widehat{f}_1''=\widehat{f}_n''=0$). In this way we construct a set of splines 'custom made' for the evaluation of the Hilbert transform.

For a discrete number N of projection angles θ, Eq. (7) yields

$$f(x_1,x_2) \sim -\frac{1}{4\pi^2 N}\left\{\sum_{j=0}^{N-1}G(x_1,x_2,\frac{2\pi j}{N})+\frac{1}{2}G(x_1,x_2,0)+\frac{1}{2}G(x_1,x_2,2\pi)\right\}, \tag{24}$$

where $G(x_1,x_2,\theta)$ denotes the evaluation of the RHS of Eq. (14) at $\rho=x_2\cos\theta-x_1\sin\theta$.

We evaluate numerically the RHS of Eq. (24) using the following steps: (i) Given ρ_i and $\widehat{f}(\rho_i,\frac{2\pi j}{N})$ we compute $\widehat{f}''(\rho_i,\frac{2\pi j}{N})$ by solving Eqs. (16a) and (16b). (ii) We compute $C(\frac{2\pi j}{N})$ using Eq. (15a). (iii) For a given (x_1,x_2), we compute ρ using Eq. (3) with $\theta=\frac{2\pi j}{N}$ and then compute $f(x_1,x_2)$ via the RHS of Eq. (24).

We have implemented the above algorithm in STIR[28], which is an object-oriented library using C++. For this purpose we have employed STIR's built-in classes *Sinogram* and *VoxelsOnCartessianGrid*. A new class, called *STR2DReconstruction*, has been created employing STIR's *AnalyticReconstruction* class in order to accommodate our algorithm.

Symmetries

In order to increase the speed of the above algorithm, we have used the following fact: Let $\{x_{1_{k_1}}\}_{k_1=1}^{sx}$, $\{x_{2_{k_2}}\}_{k_2=1}^{sy}$, $\{\rho_i\}_{i=1}^{sp}$ be uniform partitions of [-1,1], and let $\{\theta_j\}_{j=1}^{sth}$ be a uniform partition of $\left[0,\pi\frac{sth-1}{sth}\right]$. The above partitions correspond to constant detector spacing, which is the case for the Discovery ST PET system used in our implementation. Then, the eight

points

$$(x_{1_{k_1}}, x_{2_{k_2}}, \theta_j, \rho_{i+1}), \qquad (x_{1_{k_1}}, x_{2_{sx-k_2+1}}, \theta_{sth-j+2}, \rho_{i+1}),$$
$$(x_{1_{sx-k_1+1}}, x_{2_{k_2}}, \theta_{sth-j+2}, \rho_{sp-i}), \quad (x_{1_{sx-k_1+1}}, x_{2_{sy-k_2+1}}, \theta_j, \rho_{sp-i}),$$

where either $2 \leq j \leq \lceil \frac{sth}{2} \rceil$,

$$(x_{1_{k_2}}, x_{2_{k_1}}, \theta_{sth/2-j+2}, \rho_{sp-i}), \qquad (x_{1_{k_2}}, x_{2_{sx-k_1+1}}, \theta_{j-sth/2}, \rho_{sp-i})$$
$$(x_{1_{sx-k_2+1}}, x_{2_{k_1}}, \theta_{j-sth/2}, \rho_{i+1}), \qquad (x_{1_{sx-k_2+1}}, x_{2_{sx-k_1+1}}, \theta_{sth/2-j+2}, \rho_{i+1}),$$

or $\lceil \frac{sth}{2} \rceil \leq j \leq sth$,

$$(x_{1_{k_2}}, x_{2_{k_1}}, \theta_{3*sth/2-j+2}, \rho_{i+1}), \qquad (x_{1_{k_2}}, x_{2_{sx-k_1+1}}, \theta_{sth/2+j}, \rho_{i+1})$$
$$(x_{1_{sx-k_2+1}}, x_{2_{k_1}}, \theta_{sth/2+j}, \rho_{sp-i}), \qquad (x_{1_{sx-k_2+1}}, x_{2_{sx-k_1+1}}, \theta_{3*sth/2-j+2}, \rho_{sp-i}),$$

have the same $\ln|\rho - \rho_{i+1}|$ value. Thus, by executing the algorithm for k_1 from 1 to $\lceil \frac{sx}{2} \rceil$ and for k_2 from 1 to k_1, we only need to compute once the logarithm associated with the above eight points (the logarithms associated with $j = 1$ must be computed separately).

Restricting Reconstruction Within Object Boundary

Our algorithm constructs an image in a raster scan format, by scanning all pixel locations (x_1, x_2) and then calculating the integral over θ of the derivative of the half Hilbert transform, which is approximated by Eq. (14). The reconstruction time of this algorithm can be further reduced by employing object specific information that is 'hidden' in the sinogram. In this respect we consider the important case that the boundary of the object is convex. In this case, a pixel which is outside the boundary spanned by an object and hence has zero value, can be singled out from the sinogram by first identifying the detector locations for all angles θ that receive contribution from this pixel; then, for every (x_1, x_2), if there is even one θ such that $\widehat{f}(\rho, \theta) = 0$, it follows that $f(x_1, x_2)$ must be zero.

Using the above condition we can restrict the reconstruction process only to pixels within the object boundary and exclude all zero pixels outside the object. In this way, in addition to improving considerably the reconstruction time (depending on the size of the object), we can also obtain a 'clean' reconstruction without any streak artifacts outside the object. For multiple objects, such as a transverse slice of the torso including the two arms, the above approach will work for the zero pixels between the arms and the torso. This approach also

works for most of the object bounded by a concave boundary; the complete analysis of this case will be presented elsewhere.

For real data, the condition $\widehat{f}(\rho,\theta) = 0$ must be replaced by $\widehat{f}(\rho,\theta) \leq threshold$, since in the presence of system noise, pixels outside the object's boundary in the sinogram can have values greater than zero. In our implementations, the threshold value was determined manually by examining the sinogram values outside the object boundary. Various techniques for automating the threshold selection, including the minimax thresholding technique, are under investigation.

To our knowledge, sinogram thresholding has not being applied to FBP. Thresholding is not applied over the whole sinogram but it is only applied to the part of the sinogram that corresponds to points which are outside the reconstructed image. Sinogram thresholding is an optional feature of the SRT algorithm, which can be used to reduce reconstruction time, as well as to 'clean' the image.

B. The FBP algorithm

The FBP reconstruction algorithm is well known; in what follows, we briefly summarize its mathematical formulation in order to underline similarities and differences with respect to SRT. The inverse Radon transform implemented via the FBP algorithm is expressed by the following formula[34]:

$$f(x_1, x_2) = \frac{1}{N} \sum_{n=0}^{N-1} s^*(\rho, \theta_n), \tag{25}$$

where

$$s^*(\rho,\theta) = \frac{1}{2\pi} \mathcal{F}^{-1} \left[S(\xi_\rho, \theta) * H(\xi_\rho) \right], \tag{26}$$

$\mathcal{F}$ and $\mathcal{F}^{-1}$ denote the direct and inverse Fourier transform, $S(\xi_\rho,\theta)$ is the sinogram in the spatial frequency domain given by the expression

$$S(\xi_\rho,\theta) = \mathcal{F}\{\widehat{f}(\rho,\theta)\} \tag{27}$$

and the function $H(\xi_\rho)$ denotes some appropriate filter function. For our comparisons, $H(\xi_\rho)$ is a ramp filter with a cutoff frequency equal to the Nyquist frequency.

C. Simulation studies

In order to simulate the GE Discovery ST PET scanner, we have employed STIR. Briefly, the scanner consists of 24 detector rings whose diameter equals 88.62 cm. Each detector ring has 70 detector blocks, with each block consisting of an array of 6×6 crystals, giving a total of 420 crystals per ring. The generated sinograms have dimensions of 221 detectors × 210 angles. More details on this scanner can be found elsewhere[35].

In order to determine the spacial resolution of the system, a single pixel (3.195 mm) point-source has been simulated at the axial center of the FOV in two different locations: a) at the position (0 cm, 0 cm), and b) at the position (10 cm, 10 cm). After reconstructions using either SRT or FBP (without added Poisson noise), horizontal and vertical profiles were drawn through the source, and a Gaussian fit was applied in order to determine tangential and radial spatial resolution via FWHM and FWTM measurements. We note that no sinogram thresholding was applied to the SRT reconstructions. The FWHM and FWTM were calculated from the standard deviation of the fitted Gaussian. We note that this approach, employed by MacDonald *et al.*[36] and also used by Park *et al.*[37], is slightly different than the standard approach of NEMA. However, comparisons between the two approaches for determining point-source resolution has shown that the Gaussian approach is more robust with respect to pixel size variations[37].

In order to evaluate the performance of the SRT algorithm in comparison with FBP, the following 2D simulated phantoms have been used: (a) an image quality (IQ) phantom, (b) a digitized version of the Jaszczak® phantom (Data Spectrum Corporation, USA), and (c) a slice of the digital 3D Hoffman phantom[38]. For all phantoms, the image grid is of size of 128×128 pixels.

The IQ phantom simulates the human torso; it has been used in order to establish how well each algorithm can determine hot and cold lesions of variable size inside a warm background. The IQ phantom consists of two circular cold regions (with diameters of 38 mm and 32 mm) and four circular hot regions (with diameters of 25 mm, 19 mm, 15 mm, and 12 mm) inside a larger warm region that simulates the background. The radioactive concentration ratio (RCR) between hot regions and the surrounding warm background is 4:1 for the three hot regions.

The Jaszczak phantom has been used in order to investigate the ability of each algorithm

to detect cold lesions of variable size inside a radioactive background. The phantom is separated into six sections. Each section has cold circles of different size (actually these domains are rods of which a single cross-section has been analyzed) uniformly arranged to form an equilateral triangle (with circle diameters of 27.11 mm, 18.03 mm, 15.76 mm, 13.50 mm, 11.22 mm, 9.14 mm) inside a hot region of diameter 30.67 cm. The distance between rods of equal diameter is twice the diameter of the rods, center-to-center.

Finally, the Hoffman phantom simulates a cerebral PET study. It contains a complicated radioactivity distribution within small anatomical features, thus it allows the investigation of the performance of each algorithm in a more realistic situation. The Hoffman phantom contains three distinct radioactive regions: Gray Matter (GM), White Matter (WM), and Cerebrovascular Fluid (CSF). The RCR between GM and WM is 5.08:1. The radioactivity concentration in the CSF region is zero.

After placing the three simulated phantoms in the center of the scanner, 2D projection data have been generated in STIR using a ray tracing technique with 10 rays per detector. Scatter and attenuation have not been modeled. These sinograms provide the noiseless PET measurements. For each noiseless sinogram, 20 Poisson noise realizations have been generated at 5 different levels (NL1-NL5), where NL5 corresponds to the highest noise level applied. The noiseless sinograms contain 15 million events, while the noisy sinograms from NL1 to NL5 contain 75, 15, 10.5, 7.5 and 1.5 million events, respectively.

All reconstructions have been executed on a PC with Intel® Core™i7-920 Processor, running on a Linux 64-bit environment. The reconstruction grid is 221×221 for the images generated by both reconstruction algorithms. No filtering or smoothing has been applied to the SRT and FBP reconstructed images post reconstruction.

D. Real data studies

1. Imaging system and acquisition

For the preclinical data, all image acquisitions have been performed using a commercial ARGUS-CT small animal PET/CT system (SEDECAL S.A., Madrid, Spain). The PET tomograph of this system is identical to the GE Healthcare eXplore VISTA Small-Animal PET scanner which is described elsewhere[39].

All data have been acquired in a three-dimensional (3D) mode. The acquired sinograms have been corrected for deadtime, radioactivity decay, normalization, randoms, scatter, and attenuation. The scatter correction has been applied using a linear subtraction method. The attenuation correction has been performed using a transmission image segmentation technique[40]. A Fourier Rebinning Algorithm (FORE) has been applied to the 3D acquired data to produce 2D sinograms[41]. The size of each sinogram is 175 spatial locations × 128 angular samples. The FORE maximum ring difference (D_{max}) has been set to 16 and the span has been set to 3. The energy window in all studies performed is 250-700 keV.

2. Phantom studies

The spatial resolution of the system has been measured using a ^{22}Na point source (part No:MMS05-022-10U, Eckert and Ziegler, Germany) with a nominal size of 1 mm. Measurements have been acquired at two axial positions: (a) at the center of the axial FOV and (b) at 1/4 of the axial FOV away from the center of the axial FOV, at the following radial distances from the center: 0 mm, 5 mm, 10 mm, 15 mm, 20 mm, 25 mm. The acquisition time varied between 30 sec and 49 sec, collecting over 10^5 prompt counts in each position, ensuring adequate statistics. The acquired 3D sinograms have been rebinned into 2D sinograms and reconstructed using SRT and 2D FBP (ramp filter, cutoff at Nyquist frequency). The image size is 175×175 pixels, resulting in a pixel size of 0.388 mm. Tangential, radial and axial resolution measurements have been obtained by drawing line profiles though the peak intensity pixel and applying a Gaussian fit in order to determine FWHM and FWTM. No correction for source geometry have been applied.

The following two phantoms have been used: (a) a NEMA image quality phantom and (b) an in-house Derenzo phantom. A NEMA phantom (High Technology Advisors, S.L., Madrid, Spain), designed in accordance to the specifications of the NEMA NU 4-2008 quality phantom[42], has been used in order to determine the noise and contrast properties of each algorithm. This phantom is separated into three main parts: a fillable cylindrical region 30 mm in diameter and 30 mm length, a solid region with 5 fillable rods with dimensions of 1, 2, 3, 4, and 5 mm each, and a uniform region with two cold region chambers 8 mm in diameter. The entire phantom has been filled with 15.8 MBq of ^{18}F aqueous solution and one of the 8-mm cold chambers has been filled with non-radioactive water, while the other

one remained with air. A 30-min PET scan has been acquired in two bed positions.

An in-house Derenzo phantom has been used in order to test the resolution limitations of each algorithm. The Derenzo phantom consists of 31 micro capillaries (72 mm length, 6.66 μl, Hirschmann Laborgeräte, Germany) arranged in six different sectors. The inner and outer diameters of each capillary are 0.34 mm and 1 mm, respectively. The capillaries are separated by 2, 3, 4, 5, 6 and 8 mm, respectively, and there is no material between them. The phantom has been filled with 5.6 MBq of ^{18}F aqueous solution and a 60 min PET scan has been performed.

The acquired and rebinned 2D sinograms have been reconstructed using the SRT algorithm and the 2D FBP (ramp filter, cutoff at Nyquist frequency). The FBP reconstructions have been obtained using the software provided with the ARGUS-CT PET/CT commercial system, while the SRT reconstructions have been obtained via a Freemat version of the algorithm. The reconstruction matrix for both SRT and FBP is 175×175 resulting in a pixel size of 0.388 mm.

3. Animal study

In order to investigate the performance of SRT in small animal images, a one-year-old C57BL/6JOlaHsd male mouse (Harlan Interfauna Ibérica, S.L., Sant Feliu de Codines, Spain) has been imaged. The animal was kept under standard environmental conditions and had free access to food and water before the study. A 15.3 MBq of ^{18}F-FDG was administrated to the conscious mouse via intraperitoneal (ip) injection. The animal was left to rest for 60 min, and then it was anesthetized with isoflurane. Then, a 40-min PET acquisition was performed moving the animal in three bed positions. The acquired 2D sinograms were then reconstructed using the same algorithms and parameters used in the phantoms studies described above.

4. Human study

In order to investigate the performance of SRT in a clinical case, a whole-body scan of a cancer patient was acquired under a standard protocol. ^{18}F-FDG (350-400 MBq) was injected intravenously in a patient with probable pulmonary metastases. The patient was

left to rest for 60 min and whole-body PET scan was performed in 6 bed positions, using the GE Discovery ST PET/CT scanner. There was a 4-min acquisition in each bed position in two-dimensional mode. The data were reconstructed using SRT and FBP with a ramp filter, with corrections applied for random events, geometry, normalization, dead-time, scatter and attenuation.

E. Image quality metrics

For the simulated sinograms, the following quantities were calculated in order to determine the quality of the reconstructed images: (a) hot and cold region Contrast (C_{hot} and C_{cold}), (b) Coefficient of Variation (COV), (c) bias and (d) RCR. Similarly, for the real phantom images, COV and Contrast were employed. In order to determine mean activity concentration and standard deviation (which are required for the calculation of COV), as well as Contrast and RCR (see equations below), a region-of-interest (ROI) was first drawn for the noiseless image, where the boundaries between image features were clearly resolved. The same ROI was then applied for the images with noise. The mean activity concentration values within an ROI from all 20 noisy realizations were then averaged to obtain a final value. All ROIs and profile calculations have been performed using ImageJ[43] and Amide[44], both of which are open source software.

For the IQ phantom, the contrast for the four hot lesions, C_{hot}, has been determined in each noise level using the expression,

$$C_{hot} = \frac{(m_{hot}/m_{bkgd}) - 1}{(a_{hot}/a_{bkgd}) - 1}, \tag{28}$$

where m_{hot} and m_{bkgd} are the average counts measured in the hot lesion ROI and in the background ROI, respectively, averaged over all realizations (except for the case of noiseless data). The ratio (a_{hot}/a_{bkgd}) is the actual radioactivity concentration ratio between the hot lesion and the background, which in our case is 4, for all hot lesions. The contrast for the two larger cold lesions has been determined via the equation

$$C_{cold} = 1 - \frac{m_{cold}}{m_{bkgd}}, \tag{29}$$

where m_{cold} is the average counts measured in the cold lesion ROI averaged over all realizations.

The mean activities of the hot and cold regions have been determined by drawing ROIs of variable diameters for each circular region. The diameter of each circular ROI is the same as the diameter of the region being measured. In order to determine the mean activity m_{bkgd}, several larger ROIs have been drawn covering most of the background region.

The coefficient of variations has been calculated using the expression

$$COV = \frac{\sigma}{m}, \tag{30}$$

where σ and m are the standard deviation and the mean of the measured activity in the background ROI, averaged over all realizations.

The bias in the IQ phantom is defined as the mean deviation, over all realizations, of the mean pixel value within an ROI from the actual activity concentration, *i.e.*

$$bias = \left\{ \frac{1}{R} \sum_{r=1}^{R} \overline{X}_r \right\} - X_{true}, \tag{31}$$

where R is the total number of realizations, X_{true} is the true activity concentration, and $\overline{X}_r$ is the mean activity concentration within an ROI of realization r, with M number of pixels; $\overline{X}_r$ is given by

$$\overline{X}_r = \frac{1}{N} \sum_{i=1}^{N} X_i. \tag{32}$$

The calculated bias has been expressed as a percentage of the true activity concentration of the lesion been measured, X_{true}.

In order to create contrast vs. noise and bias vs. noise plots after smoothing, 20 new noisy realizations at a noise level higher than NL5 have been created (750 thousand events). Each image obtained after reconstruction with either SRT or FBP, was blurred with a Gaussian filter of six different sizes (2×2, 3×3, 4×4, 5×5, 7×7 and 12×12 pixels). ROI measurements were then performed for each realization and the average (over all realizations) contrast was calculated for each lesion using either Eq. (28) or Eq. (29), depending on the type of lesion. Furthermore, the bias was calculated using Eq. 31 and expressed as a percentage of the actual pixel value for the hot regions, and as number of counts for the cold regions.

In the Jaszczak phantom, the contrast in each noise level has been determined in the cold regions with respect to the radioactive background using Eq. (29). The mean activity m_{cold} has been determined in four of the six sections by drawing ROIs as close as possible to the actual size of each rod, in all rods composing each sections. The contrast for the

two smallest regions has not been determined since in this case due to the small size of each rod, it is difficult to define a ROI. The mean activity of the radioactive background is determined by drawing multiple smaller ROIs between the rods been measured, throughout the radioactive region. The COV for the Jaszczak phantom is calculated using Eq. (30).

In order to determine the capability of each reconstruction algorithm to resolve the closely separated rods of the Jaszczak phantom, the noisy reconstructed images were first averaged over all reconstructed realizations. Then, line profiles were drawn through the rods of each section of the phantom, for each noise level. The line profile acquired from the reconstruction image of each algorithm has been normalized to the maximum value of each profile.

In the Hoffman phantom, the contrast between GM and CSF, as well as the contrast between WM and CSF, have been determined using Eq. (29), where m_{cold} corresponds to the mean value obtained from the CSF region and m_{bkgd} corresponds to the mean value obtained from either the WM or the GM region. The COV is determined from the WM using Eq. (30). The RCR between GM and WM is determined from the following expression

$$RCR = \frac{m_{GM}}{m_{WM}}, \tag{33}$$

where m_{GM} and m_{WM} are the average counts measured in ROI_{GM} and ROI_{WM}, averaged over all realizations. In order to determine the mean activities in these areas, multiple small circular ROIs have been drawn throughout the image in each corresponding region and the mean value has been calculated.

Furthermore, the bias in the SRT and FBP reconstructed Hoffman images has been calculated for both the WM and GM using Eq. (31).

For the real data collected from the NEMA NU 4-2008 image quality phantom, the COV has been calculated from a slice of the uniform region. The mean activity and standard deviation have been determined by drawing a 27-mm ROI (over 95% of the active region) and the COV has been calculated using Eq. (30).

The contrast, C_{cold} between air and radioactive region, as well as between water and radioactive region, have been determined from a slice of the two cold chambers. The mean activities in these regions have been obtained by drawing a 7.75-mm ROI (over 90% the physical diameter of the cylinders) over the air-filled and water-filled chambers, and a larger ROI over the radioactive region. The contrast between the two cold regions and the radioactive region have been calculated using Eq. (29).

TABLE I. Point-source spatial resolution measurements for simulated data.

At axial center at position (0 cm,0 cm)				
Profile	Parameters	SRT	FBP	Improvement
Radial	FWHM	4.88 mm	5.29 mm	7.75%
	FWTM	8.89 mm	9.64 mm	7.78%
Tangential	FWHM	4.88 mm	5.30 mm	7.92%
	FWTM	8.89 mm	9.66 mm	7.97%
At axial center at position (10 cm,10 cm)				
Profile	Gaussian Fit Parameters	SRT	FBP	Improvement
Radial	FWHM	4.66 mm	4.84 mm	3.72%
	FWTM	8.50 mm	8.82 mm	3.63%
Tangential	FWHM	4.64 mm	4.80 mm	3.33%
	FWTM	8.45 mm	8.75 mm	3.43%

The contrast for each section of the Derenzo phantom has been calculated using Eq. (29). The mean activities in each section have been obtained by drawing circular ROIs of a diameter close to the actual diameter of the lesion, in all lesions of each section of the phantom. In order to determine the mean activity of the background, multiple ROIs have been drawn between the hot lesions of each section. Furthermore, in order to determine the capability of each reconstruction algorithm to resolve the closest separated capillaries of the Derenzo phantom, a line profile through a row of the 2-mm separated spots has been drawn. The line profile acquired from the reconstruction image of each algorithm is normalized to the maximum value of each profile.

III. RESULTS

The reconstruction time for SRT depends on the size of the sinogram and the reconstruction grid. By restricting reconstruction within the object boundaries via sinogram thresholding, the reconstruction time decreases depending on the size of the object being imaged. For the simulated Hoffman phantom (sinograms of size 221×210, and 221×221 reconstruction grid), the reconstruction time is about 2.1 sec per sinogram, executed on a PC with Intel® Core™i7-920 Processor. We note that no parallel programming or other accelerating techniques have been employed. The corresponding reconstruction time for FBP in STIR is about 0.3 sec.

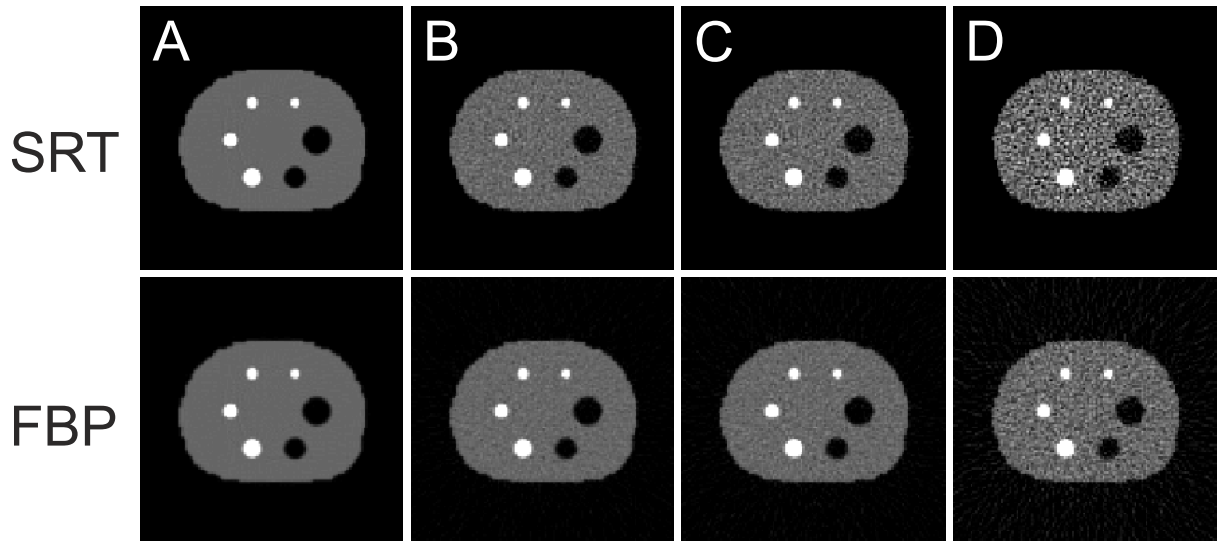

FIG. 1. Reconstructed images of the simulated IQ phantom at various noise levels (the noise level increases moving from left to right): (A) No Noise, (B) Noise Level 2, (C) Noise Level 4 and (D) Noise Level 5.

A. Simulation studies

Table I presents the spatial resolution properties (FWHM and FWTM), in the radial and tangential directions, for the SRT and FBP reconstructed point-source images, simulated at two different radial locations. These results indicate an improvement in FWHM and FWTM of almost 8% at the center of the scanner, and a smaller improvement, about 3.5% at the position (10 cm,10 cm).

For the IQ simulated phantom, comparisons between SRT and FBP reconstructed images with no noise, as well as with noise (NL2, NL4 and NL5) are shown in Fig. 1. For economy of presentation, images from NL1 and NL3 are not shown. The noisy images presented are representative reconstructions of one realization at the specific noise level. Both SRT and FBP can generate negative values in pixels where the value of the original phantom is very low or zero. In all images presented, the all-black color corresponds to zero values. The value for the all-white color is chosen in order to enhance the contrast of the figures and to emphasize some of the streak artifacts. Both reconstructions are displayed on the same scale.

Although, the reconstructions from both methods appear similar, there exist two main

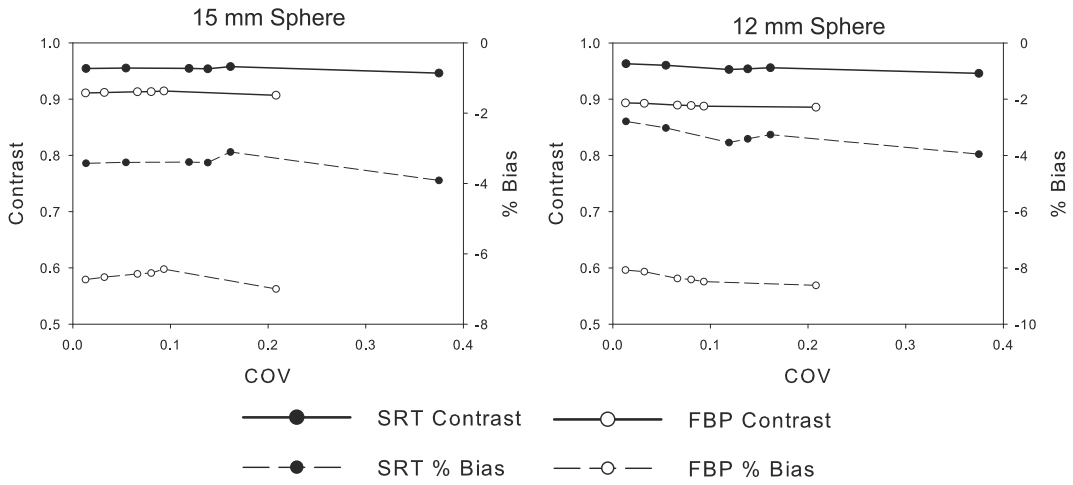

FIG. 2. Contrast and bias vs. COV for the two reconstruction algorithms obtained from the reconstructed images of the simulated IQ Phantom. Note that the leftmost data point in each curve corresponds to the noiseless case, while the rightmost data point corresponds to the NL5 case.

differences: From visual inspection it is clear that there exist differences in noise texture between SRT and FBP reconstructions. Specifically, the reconstructions obtained from SRT appear more noisy than those obtained from FBP at every noise level. Furthermore, the SRT reconstructions are completely clear from streak artifacts outside the object, whereas some small streak artifacts are present in FBP reconstructions.

The contrast, C_{hot}, for the two smallest hot spheres of the IQ phantom (15 mm, and 12 mm) as a function of COV, is presented in Fig. 2. The SRT algorithm exhibits higher contrast in all three lesions independently of noise level. The improvement in contrast over FBP increases as the size of the lesion decreases. Indeed, we observe no differences in C_{cold} for the 38-mm and 32-mm cold spheres, but a small SRT improvement in C_{hot} for the 25-mm lesion and larger improvement for the 19-mm lesion (graphs not shown).

The percent bias generated by the reconstruction algorithms, for the two smaller hot lesions as a function of noise level, is also presented in Fig. 2. The bias is negative in all cases. There are no significant differences in bias between SRT and FBP for the cold lesion and for the largest hot lesion (graphs not shown). The bias had small variations as a function of COV for both SRT and FBP. FBP appears to give a higher bias in all cases reaching about 9% for the 12-mm lesion. The percent bias for FBP increases as the lesion

size decreases. The percent bias for SRT has small variations as a function of lesion size. Similar plot has been obtained for the 19-mm hot lesion (graph not shown).

Contrast vs. noise and bias vs. noise plots after smoothing are presented in Fig. 3 for the 32-mm cold lesion as well as for the three smaller hot lesions. Similar plots have been obtained for the remaining two lesions (graphs not shown). For the cold lesions, the curves between SRT and FBP are similar, and both reconstruction methods yield over 88% contrast. The bias for the cold region is very small for both algorithms (varies for 1 to 8 counts), and increases as the size of the Gaussian filter increases. For the hot lesions, there is a similar behavior of contrast and bias for SRT and FBP after smoothing. However, there is a shift of the SRT curve towards higher noise, yielding at the same time higher contrast and lower bias values than FBP. For example, for the 12-mm hot lesion the contrast improves (without smoothing) from 87% with FBP to 97% with SRT, and the bias from -10% with FBP to -2.5% with SRT, at the expense of noise.

For the Jaszczak simulated phantom, comparisons between SRT and FBP reconstructed images with no noise, as well as with noise (NL2, NL4 and NL5) are shown in Fig. 4. The noisy images presented are representative reconstructions of one realization at the specific noise level. Similarly to the IQ phantom, the SRT images are more noisy than the images obtained from FBP. However, the SRT reconstruction provides images without any streak artifacts outside the object, whereas small streak artifacts are present in the FBP reconstructions, especially in NL5. Both SRT and FBP reconstructions are capable of resolving visually the smallest rods (9.14-mm in diameter) in all noise levels.

Fig. 5 presents contrast comparisons between SRT and FBP as a function of noise level for the 15.76-mm and 13.50-mm rods of the Jaszczak phantom. The SRT algorithm presents a small improvement (2-5%) over FBP in C_{cold} in all noise levels for the two rod sizes displayed. Similar plot has been obtained for the 18.03-mm rod, however there is no difference in contrast for the largest (27.11-mm) rod (graphs not shown). The contrast for the two smaller regions (11.22-mm and 9.14-mm) could not be determined.

Fig. 6 illustrates the line profiles obtained along the 9.14-mm rods of the Jaszczak phantom with no noise, as well as with noise (NL2, NL4 and NL5). The improved contrast of SRT is clearly illustrated. Similar plots have been obtained from the other sections of the phantom.

For the Hoffman simulated phantom, comparisons between SRT and FBP reconstructed

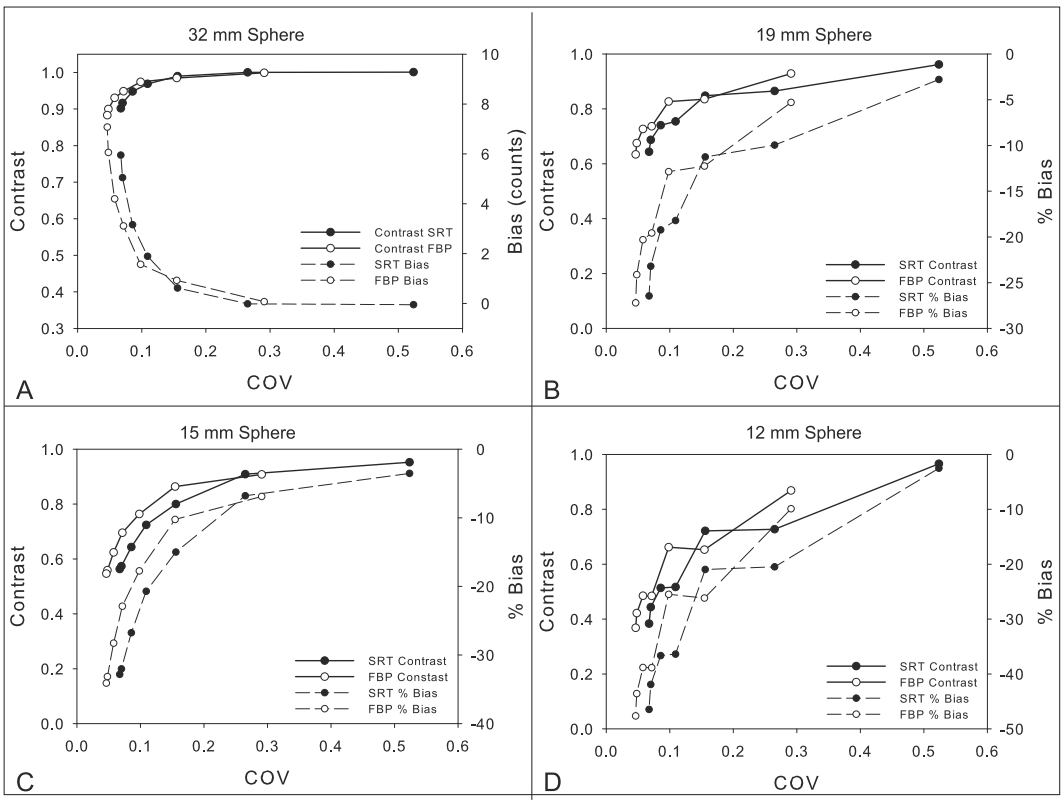

FIG. 3. Contrast and bias vs. COV after Gaussian blurring for: A) 32-mm cold sphere, B)19-mm hot sphere, C) 15-mm hot sphere and D) 12-mm hot sphere. The leftmost data point in each curve corresponds to the case of no blurring, while the rightmost data point corresponds to the case of blurring with a 12×12 pixels Gaussian window. Note that the bias for the cold-sphere case is presented as number of counts.

images with no noise, as well as with noise (NL2, NL4 and NL5) are shown in Fig. 7. The noisy images presented are representative reconstructions of one realization at the specific noise level. All anatomical features of this phantom can clearly be identified for all selected noise levels by both algorithms. Small streak artifacts outside the object are present in the FBP reconstructions, whereas the SRT reconstruction provides images with no such artifacts.

Contrast plots between GM/CSF and WM/CSF as a function of noise level are presented in Fig. 8(A) and Fig. 8(B). We observe a small improvement in contrast for the SRT algorithm especially for the case of the WM. RCR plots comparing the two reconstruction algorithms as a function of noise level are presented in Fig. 8(C). The RCR calculations

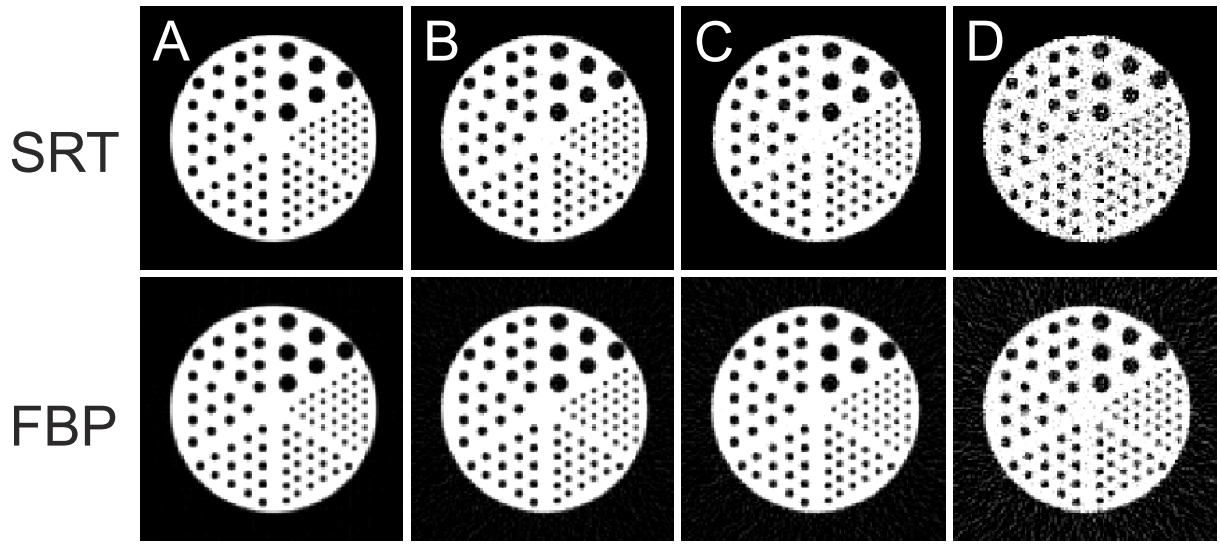

FIG. 4. Reconstructed images of the simulated Jaszczak phantom at various noise levels: (A) No Noise, (B) Noise Level 2, (C) Noise Level 4 and (D) Noise Level 5.

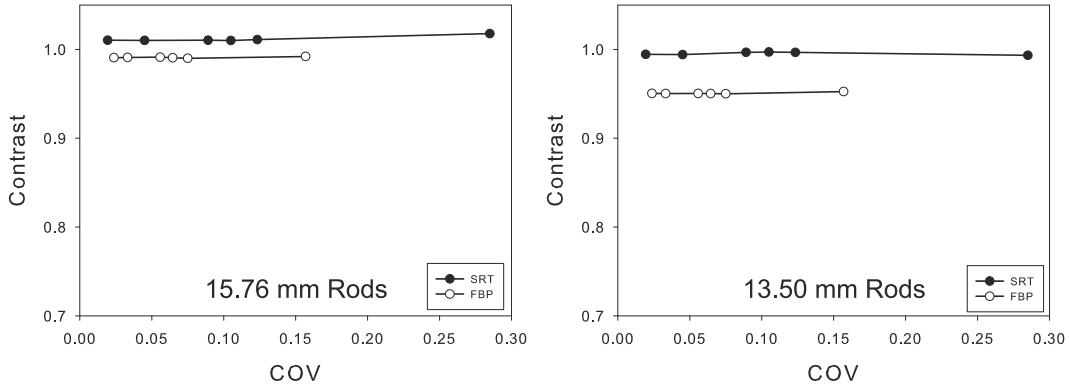

FIG. 5. Contrast vs. COV for the two reconstruction algorithms for two sections of the simulated Jaszczak phantom. Note that the leftmost data point in each line curve corresponds to the noiseless case, while the rightmost data point corresponds to the NL5 case.

between GM and WM suggest that FBP slightly underestimates the actual RCR value (dotted line), whereas the RCR calculated from SRT reconstructions is closer to the actual value. The percent bias for the GM as a function of noise level is depicted in Fig. 8(D). There is a negative bias in both algorithms, similar to the case of the IQ phantom. The bias is 4% for the FBP and about 2% for the SRT algorithm. The bias for the GM was under 0.8% for both algorithms (graph not shown).

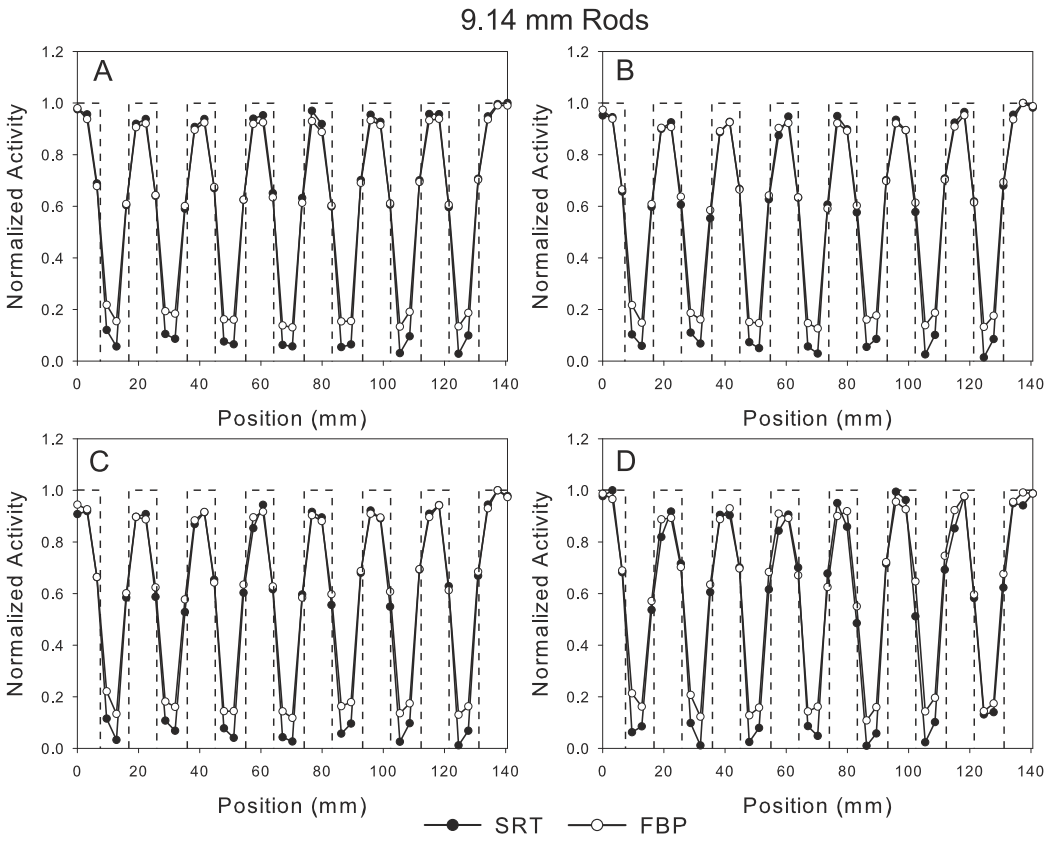

FIG. 6. Line profiles obtained along the 9.14-mm rods of the Jaszczak phantom for four levels of noise: (A) No Noise, (B) NL2, (C) NL4 and (D) NL5. The dashed lines correspond to normalized profile values through the simulated phantom

B. Real data studies

Table II summarizes the spatial resolution properties (FWHM and FWTM), in the radial, tangential and axial directions, for the SRT and FBP reconstructed images of the ^{22}Na point source, at various axial and radial locations. The results indicate that there is no significant difference between SRT and FBP in the axial direction. However, in the radial and tangential directions there is a small but consistent improvement with SRT that reaches about 4% in one radial location.

Reconstructed images obtained via SRT and FBP (including SRT without sinogram thresholding) of three slices of the NEMA NU 4-2008 image quality phantom, are presented in Fig. 9. Small streak artifacts are present in both SRT and FBP reconstructions. These artifacts are reduced in SRT when sinogram thresholding is applied.

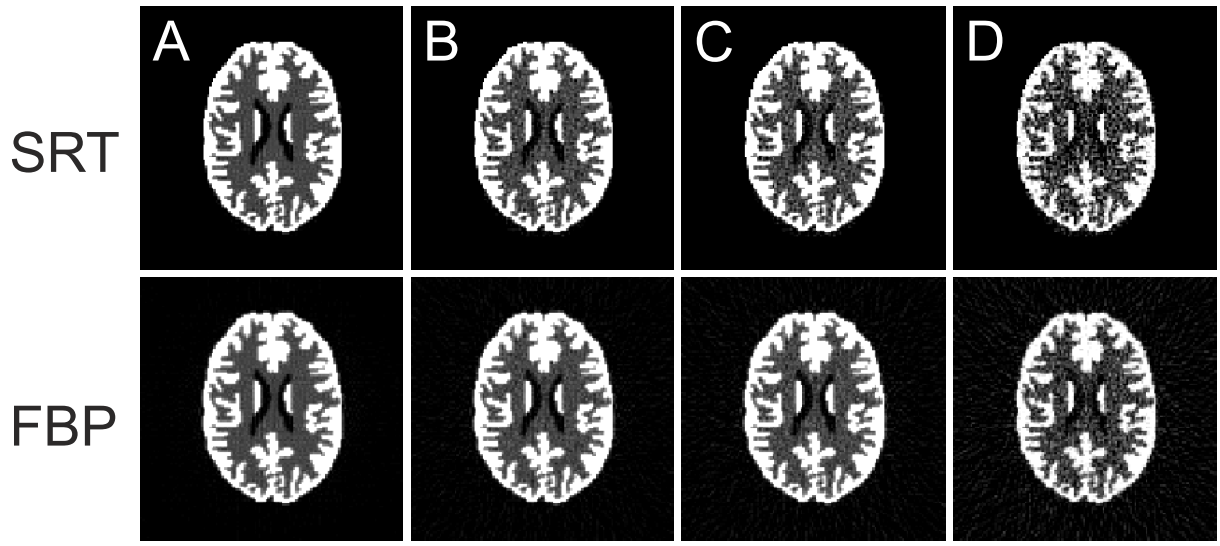

FIG. 7. Reconstructed images of the simulated Hoffman phantom at various noise levels: (A) No Noise, (B) NL2, (C) NL4 and (D) NL5.

COV and contrast calculations using the uniform slice and the cold chamber slice of the NEMA phantom, are presented in Fig. 10 (A and B). The SRT reconstructed images exhibit slightly higher COV values in comparison to FBP. The contrast values for both the water and air chambers are similar for both algorithms.

Reconstructed images of the Derenzo phantom are shown in Fig. 9. All reconstructed circular sources are clearly visible with both methods. Fig. 10(C) illustrates the contrast for the various sectors of the Derenzo phantom calculated from the SRT and FBP reconstructed images. The contrast in the SRT reconstructed images is higher than FBP; the difference between SRT and FBP becomes larger, as the center-to-center spacing between the lesions of the Derenzo phantom becomes smaller. Fig. 10(D) illustrates the line profiles obtained along the 2-mm separated capillaries of the phantom. SRT resolves the 2-mm separated holes slightly better that FBP.

Reconstructed images of four representative transaxial slices of the ^{18}F-FDG mouse study, are presented in Fig. 11. Each column of the image mosaic represents distinct anatomical features: from left to right, (a) a slice through the abdomen (liver) and spine cord, (b) a slice through the thoracic cavity, (c) a slice though the thoracic cavity including the heart, (d) a slice though the Hyoid bone in the upper cervical area.

Reconstructed images of a representative transaxial slice though the thoracic cavity of

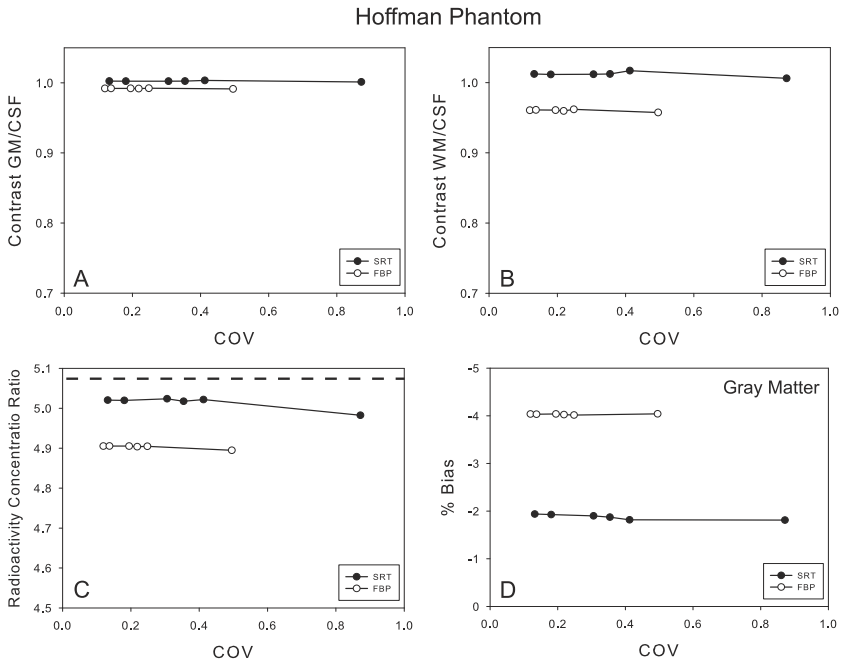

FIG. 8. Contrast, RCR and bias vs. COV comparisons between the two reconstruction algorithms for the simulated Hoffman phantom. Contrast was determined for GM with respect to CSF (A) and for WM with respect to CSF (B). RCR between GM and WM was also determined (C). The dashed line indicates the actual RCR between GM and WM of the simulated Hoffman phantom being imaged. The bias is presented as a percentage of the true activity concentration of the lesion been measured (D). Note that the leftmost data point in each line curve corresponds to the noiseless case, while the rightmost data point corresponds to the NL5 case.

the ^{18}F-FDG whole-body PET study are presented in Fig. 12 using SRT (with and without sinogram thresholding) and FBP with a ramp filter. Furthermore, the same reconstructions are also presented after applying a 4×4 pixel Gaussian post-reconstruction filter. The four lesions present in the lung of the patient are clearly visible in both reconstructions. A small improvement in contrast and resolution appears in the SRT reconstructions. However, the noise level of SRT is slightly higher in comparison to FBP.

IV. DISCUSSION

In this work, a new analytic image reconstruction technique, the SRT, has been evaluated in comparison to FBP under PET imaging conditions using simulated and real data. The

TABLE II. Point source resolution measurements for real data.

		At axial center											
		0 mm		5 mm		10 mm		15 mm		20 mm		25 mm	
		FWHM	FWTM	FWHM	FWTM	FWHM	FWTM	FWHM	FWTM	FWHM	FWTM	FWHM	FWTM
Radial	SRT	1.57	2.86	1.69	3.08	1.83	3.33	1.91	3.48	2.07	3.77	2.3	4.2
	FBP	1.6	2.92	1.74	3.18	1.87	3.40	1.97	3.59	2.11	3.84	2.33	4.24%
	Improvement	1.88%	2.05%	2.87%	3.14%	2.14%	2.06%	3.05%	3.06%	1.90%	1.82%	1.29%	0.94%
Tangential	SRT	1.44	2.62	1.46	2.66	1.42	2.59	1.39	2.53	1.56	2.84	1.56	2.85
	FBP	1.45	2.64	1.50	2.74	1.46	2.67	1.43	2.61	1.60	2.92	1.61	2.93
	Improvement	0.69%	0.76%	2.67%	2.92%	2.74%	3.00%	2.80%	3.07%	2.50%	2.74%	3.11%	2.73%
Axial	SRT	1.32	2.40	1.72	3.14	1.88	3.43	2.02	3.68	2.23	4.06	2.60	4.73
	FBP	1.32	2.41	1.73	3.15	1.87	3.41	2.03	3.71	2.23	4.06	2.60	4.73
	Improvement	0.00%	0.41%	0.58%	0.32%	-0.53%	-0.59%	0.49%	0.81%	0.00%	0.00%	0.00%	0.00%

		At 1/4 axial FOV from center											
		0 mm		5 mm		10 mm		15 mm		20 mm		25 mm	
		FWHM	FWTM	FWHM	FWTM	FWHM	FWTM	FWHM	FWTM	FWHM	FWTM	FWHM	FWTM
Radial	SRT	1.62	2.94	1.65	3.01	1.90	3.45	2.02	3.68	2.12	3.86	2.52	4.58
	FBP	1.64	2.98	1.69	3.08	1.96	3.56	2.10	3.83	2.12	3.86	2.52	4.6
	Improvement	1.22%	1.34%	2.37%	2.27%	3.06%	3.09%	3.81%	3.92%	0.00%	0.00%	0.00%	0.43%
Tangential	SRT	1.47	2.67	1.38	2.51	1.43	2.60	1.41	2.57	1.63	2.97	1.63	2.97
	FBP	1.47	2.68	1.43	2.60	1.47	2.68	1.46	2.65	1.67	3.05	1.68	3.05
	Improvement	0.00%	0.37%	3.50%	3.46%	2.72%	2.99%	3.42%	3.02%	2.40%	2.62%	2.98%	2.62%
Axial	SRT	1.28	2.34	1.63	2.98	1.57	2.87	1.67	3.04	1.77	3.22	1.93	3.51
	FBP	1.29	2.34	1.64	2.99	1.58	2.87	1.67	3.05	1.78	3.25	1.93	3.51
	Improvement	0.78%	0.00%	0.61%	0.33%	0.63%	0.00%	0.00%	0.33%	0.56%	0.92%	0.00%	0.00%

algorithm has been implemented in the STIR Open Source software library; by employing several symmetries, the reconstruction time has been reduced drastically in comparison to an earlier version[29]. Further improvement in reconstruction time can be accomplished by a sinogram thresholding option which restricts reconstruction within object boundaries. The performance of the algorithm has been assessed by analyzing a variety of measures of merit including resolution (via FWHM and FWTM), contrast for cold and hot regions, radioactivity concentration ratio between two regions and bias. Overall, regarding the simulation

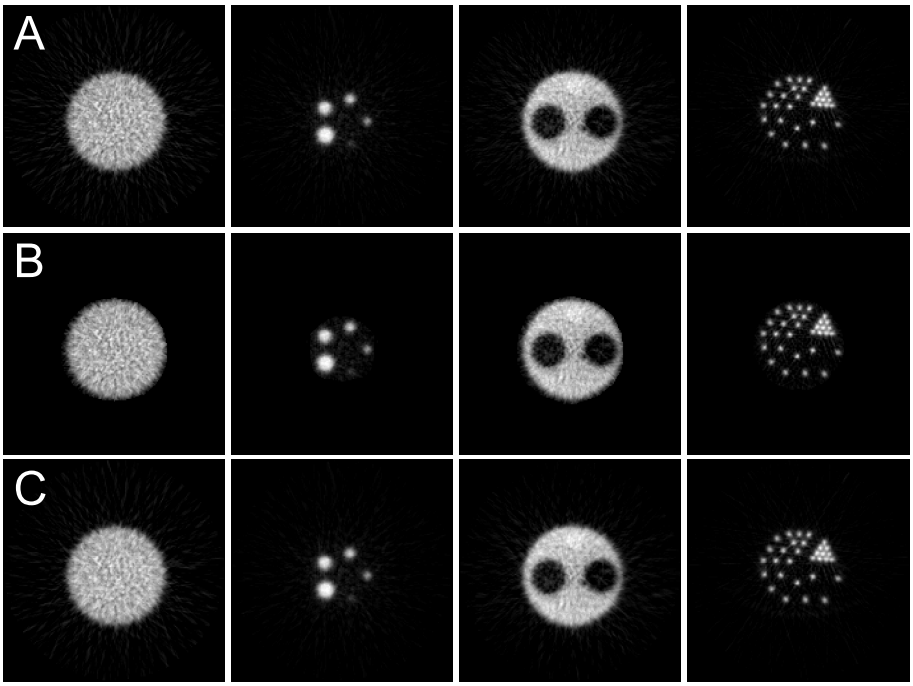

FIG. 9. Reconstructions of three slices of the NEMA NU 4-2008 image quality phantom and a slice of the Derenzo phantom, acquired by the ARGUS-CT small animal PET/CT system: (A) SRT with no thresholding, (B) SRT with thresholding, (C) FBP with a ramp filter. Note that the 8-mm cold chamber on the left of the NEMA 2 slice is filled with non-radioactive water and the one on the right with air.

studies, SRT provided images of higher resolution, higher contrast and lower bias than FBP. Regarding the real studies, SRT provides a small increase in resolution and contrast especially for the closely spaced 2-mm lesions of the Derenzo phantom. The above improvements are apparently the consequence of increasing slightly the noise in the reconstructed images.

The contrast vs. noise and bias vs. noise plots after smoothing demonstrate similar behavior between SRT and FBP. However, SRT by producing a noisier image without smoothing, it provides a larger range of COV values to choose from (one could argue that by selecting a cutoff frequency higher than the Nyquist frequency one could achieve higher COV for FBP and therefore one could improve contrast and bias; however, at these higher frequencies the images suffer from aliasing and STIR, as well as other reconstruction packages, do not allow this option).

Our reconstruction technique is different than FBP, or other analytic formulae for parallel

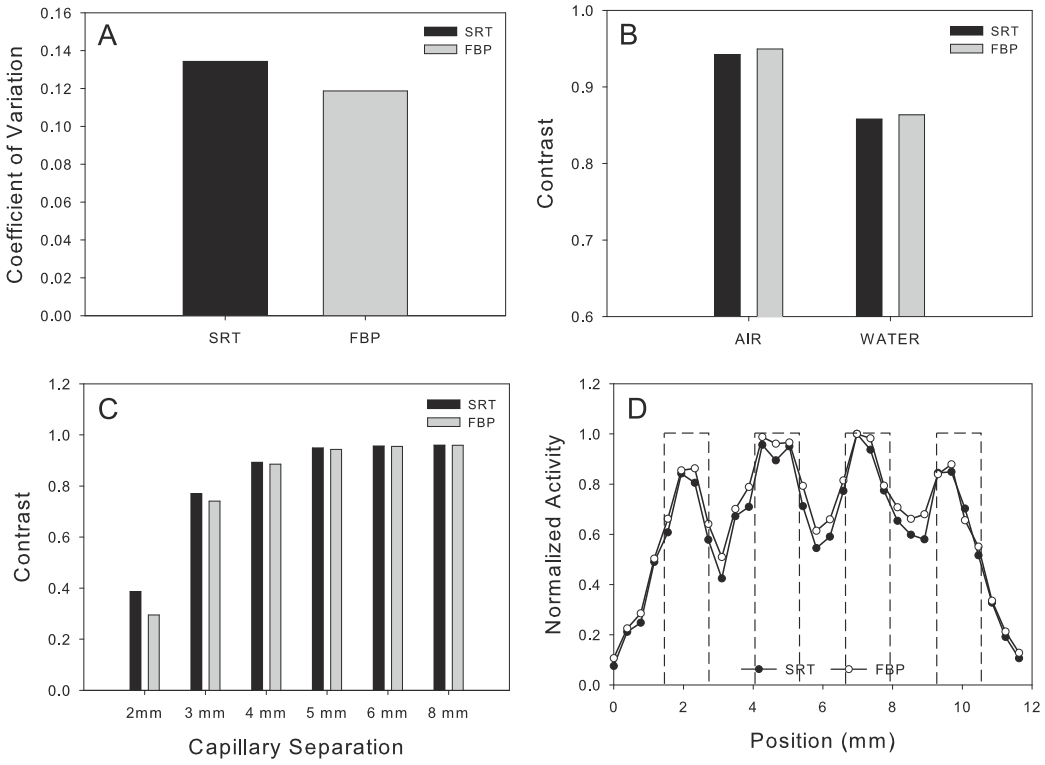

FIG. 10. Results from analyzing real NEMA NU 4-2008 and Derenzo phantom images: (A) COV, (B) Contrast for water-to-background and air-to-background, (C) Contrast for the different sections of the Derenzo phantom and (D) Line profiles obtained along the 2-mm separated capillaries of the Derenzo phantom. The dashed lines corresponds to normalized profile values through the actual phantom.

projections that have appeared in the literature the last 15 years, including the direct analytic inversion formulae of Clackdoyle *et al.*[45], Clackdoyle and Noo[46], and Defrise *et al.*[47]. In the case of FBP, images are obtained by backprojecting appropriately filtered projection data. This approach involves the direct Fourier transform of the projection data and the inverse Fourier transform of the filtered projection followed by the backprojection step. Another important analytical technique is the two-step Hilbert transform method developed by Noo *et al.*[48]. This method involves the backprojection of the derivative of the projection data and the recovery of the image using Hilbert transform techniques. The advantage of this approach is the ability to obtain ROI reconstructions from truncated projections. In the approach developed by Zeng[49], the order of backprojection and differentiation of the two-step

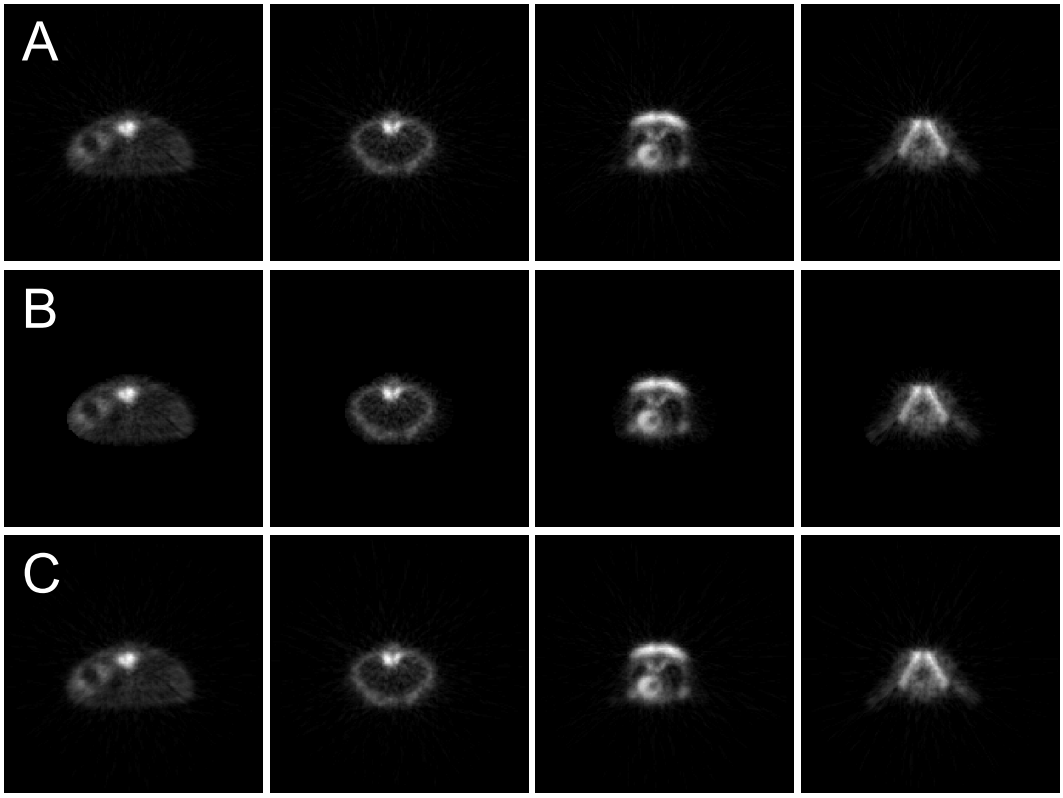

FIG. 11. Reconstructions of four representative slices of a mouse study acquired by the ARGUS-CT small animal PET/CT system: (A) SRT with no thresholding, (B) SRT with thresholding, (C) FBP with a ramp filter.

Hilbert transform is reversed.

In contrast to the above techniques, the SRT involves the backprojection of the derivative of the Hilbert transform of the projection data. The derivative of the Hilbert transform is computed analytically by expanding the projection data in each interval in terms of 'custom made' cubic splines.

A similar approach was employed by La Rivière and Pan (La Rivière and Pan 1998) in which cubic spline functions were fitted to the projection data. However, both the final formulation and the numerical implementation of the above authors are substantially different than ours (in particular, their inversion formula involves the numerically unstable term $\ln\left(\frac{\xi'-\xi_i}{\xi'-\xi_{i+1}}\right)$). In spite of these differences, the improvement of spatial resolution obtained via SRT is in agreement with the results obtained by La Rivière and Pan (La Rivière and Pan 1998) using SPECT data. Apparently, this improvement is a direct consequence of

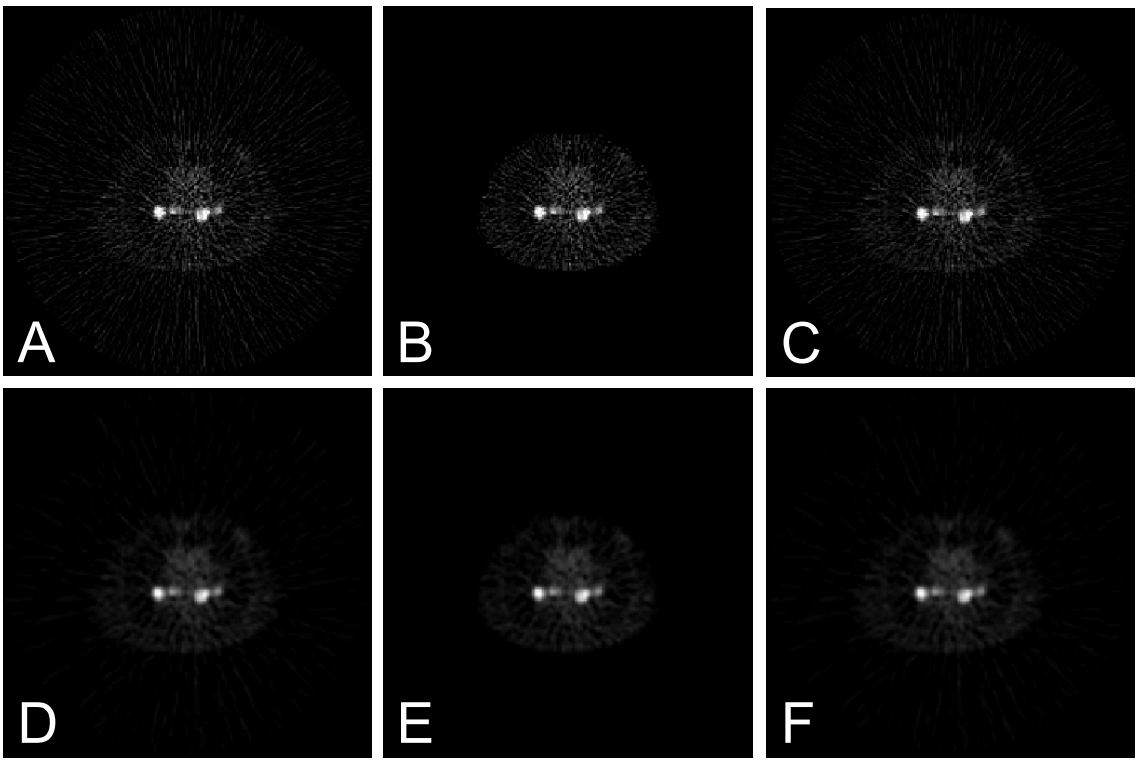

FIG. 12. Reconstructions of a representative slice through the chest area of a whole-body PET scan acquired by the GE Discovery ST PET/CT scanner: (A) SRT with no thresholding, (B) SRT with thresholding, (C) FBP with a ramp filter, (D) SRT with no thresholding and Gaussian smoothing, (E) SRT with thresholding and Gaussian smoothing, (F) FBP with a ramp filter and Gaussian smoothing.

the way that these two approaches treat the projection data. Indeed, since the sinogram is known on a finite grid, the Radon transform can not be inverted using FBP without the discrete filtration and backprojection steps. This discrete approximation of the inverse Radon transform used in FBP, is avoided in the splines technique where the sinogram is treated as a continuous function. By fitting an analytic expression to the discretized projection data, a closed-form expression for the quantity that must be backprojected can be computed, thus eliminating the need for interpolation before backprojection.

FBP suppresses high frequencies in the projection data and perhaps this results in lower resolution images than these obtained with SRT. Indeed, since the high-frequency components carry more noise, the SRT reconstructions appear more noisy than those of FBP. In summary, the improvement of the spatial resolution of SRT in comparison with FBP is re-

lated to the fact that SRT is formulated in the physical space, whereas FBP is formulated in the Fourier space.

The SRT algorithm can also be applied to other imaging modalities such as CT and SPECT. In this latter case, which involves a rotating camera, SRT has the capability of providing effective reconstructions for truncated sinograms. A detailed analysis of truncated geometries and ROI reconstructions will be presented elsewhere.

It is important to note that SRT does *not* require a sinogram with evenly spaced angles and detectors, it only requires a sinogram with known detector locations and projection angles. Thus, SRT *can* accommodate complicated system geometries with variable detector spacing; details will be presented elsewhere.

OSEM is now in widespread use in clinical and preclinical systems. The comparison of SRT with iterative algorithms is work in progress, and the relevant results will be presented in the near future. Preliminary studies indicate that SRT has certain advantages, particularly in cases where quantification of radioactivity is required.

FBP is currently the only analytic reconstruction algorithm available through the STIR library. It appears that SRT provides a good alternative to FBP, especially now that the speed of SRT is comparable to that of FBP. Therefore, we intend to make the reconstruction code for SRT part of the STIR open source library, which will allow many users to explore particular advantages of SRT.

V. CONCLUSIONS

In this work, we have presented the evaluation of SRT, a novel, analytic, 2D, image reconstruction technique for parallel beam geometry. This algorithm has been evaluated using simulated and real PET data, in comparison to FBP. Overall, the SRT provides images of higher resolution, higher contrast and lower bias than FBP; apparently this is achieved by increasing slightly the noise in the reconstructed images. Unlike other analytic reconstruction algorithms, the reconstruction time of SRT is comparable with that of FBP. The implementation of SRT to simulated and real SPECT data will be presented elsewhere. Taking into consideration that SRT improves resolution by increasing noise, it is natural to speculate that SRT may also be useful for CT, where the data contain less noise. In future studies, an oriented imaging-task analysis will be performed and the usefulness of

this algorithm under specific clinical tasks will be rigorously analyzed.

ACKNOWLEDGMENTS

The authors would like to thank George Kontaxakis and Konstantinos Karaoglanis for their assistance and Ioannis Datseris and the staff of the PET/CT Unit of "Evangelismos" General Hospital for providing the clinical data. A. S. Fokas gratefully acknowledges support from the EPSRC, UK (Grant No EP/H051309/1), and from the John Simon Guggenheim Memorial Foundation, USA. UCL/UCH receives research support from the NIHR Biomedical Research Centres funding scheme.

---

* Author to whom correspondence should be addressed. E-mail: gkastis@academyofathens.gr

† Centre for Medical Radiation Physics, University of Wollongong, NSW, Australia

‡ Research Center of Mathematics, Academy of Athens, Soranou Efessiou 4, Athens 11527, Greece

[1] G. D. Hutchins, M. A. Miller, V. C. Soon, and T. Receveur, "Small animal PET imaging," ILAR J. **49**(1), 54–65 (2008).

[2] J. M. U-King-Im, V. Young, and J. H. Gillard, "Carotid-artery imaging in the diagnosis and management of patients at risk of stroke," Lancet Neurol. **8**(6), 569–580 (2009).

[3] D.-M. Koh, G. J. R. Cook, and J. E. Husband, "New horizons in oncologic imaging," N. Engl. J. Med. **348**(25), 2487–2488 (2003).

[4] J. Czernin, M. Allen-Auerbach, and H. R. Schelbert, "Improvements in cancer staging with PET/CT: literature-based evidence as of September 2006," J. Nucl. Med. **48**(1), 78S–88S (2007).

[5] L. Fass, "Imaging and cancer: A review," Mol. Oncol. **2**(2), 115–152 (2008).

[6] S. R. Cherry and S. S. Gambhir, "Use of positron emission tomography in animal research," ILAR J. **42**(3), 219–232 (2001).

[7] A. J. Lucas, R. C. Hawkes, R. E. Ansorge, G. B. Williams, R. E. Nutt, J. C. Clark, T. D. Fryer, and T. A. Carpenter, "Development of a combined microPET-MR system," Technol. Cancer Res. Treat. **5**(4), 337–341 (2006).

[8] S. R. Cherry, "Fundamentals of positron emission tomography and applications in preclinical drug development," J. Clin. Pharmacol. **41**(5), 482–491 (2001).

[9] A. C. Kak and M. Slaney, *Principles of computed tomographic imaging* (IEEE Press, New York, 1988).

[10] B. F. Hutton, J. Nuyts, and H. Zaidi, "Iterative reconstruction methods," H. Zaidi ed *Quantitative analysis in nuclear medicine imaging* (Springer, New York, 2006), pp. 107–140.

[11] B. M. W. Tsui and E. C. Frey, "Analytic image reconstruction methods in emission computed tomography," H. Zaidi ed *Quantitative analysis in nuclear medicine imaging* (Springer, New York, 2006), pp. 82–106.

[12] P. P. Bruyant, "Analytic and iterative reconstruction algorithms in SPECT," J. Nucl. Med. **43**(10), 1343–1358 (2002).

[13] M. Defrise and G. T. Gullberg, "Image reconstruction," Phys. Med. Biol. **51**(13), R139–R154 (2006).

[14] J. Radon, "Uber die Bestimmung von Funktionen durch ihre Integralwerte langs gewisser Mannigfaltigkeiten," Ber. Verh. Sachs. Akad. Wiss. **69**, 262–277 (1917).

[15] J. Radon, "On the determination of functions from their integral values along certain manifolds," IEEE Trans. Med. Imag. **5**(4), 170–176 (1986).

[16] A. M. Cormack, "Representation of a function by its line integrals, with some radiological applications," J. Appl. Phys. **34**, 2722–2727 (1963).

[17] H. H. Barrett, "The Radon transform and its applications," *Progress in Optics XXI*, E. Wolf ed (Elsevier, Amsterdam, 1984).

[18] L. A. Shepp and Y. Vardi, "Maximum likelihood reconstruction for emission tomography," IEEE Trans. Med. Imag. **1**(2), 113–121 (1982).

[19] M. Hudson and R. S. Larkin, "Accelerated image reconstruction using ordered subsets of projection data," IEEE Trans. Med. Imag. **13**(4), 601–609 (1994).

[20] R. E. Carson, Y. Yan, B. Chodkowski, T. K. Yap, and M. E. Daube-Witherspoon, "Precision and accuracy of regional radioactivity quantitation using the maximum likelihood EM reconstruction algorithm," IEEE Trans. Med. Imag. **13**(3), 526–537 (1994).

[21] C. A. Johnson, Y. Yan, R. E. Carson, R. L. Martino, and M. E. Daube-Witherspoon, "A system for the 3D reconstruction of retracted-septa PET data using the EM algorithm," IEEE Trans. Nucl. Sci. 42(4), 1223–1227 (1995).

[22] F. A. A. De Jonge and K. A. K. Blokland, "Statistical tomographic reconstruction: How many more iterations to go?," Eur. J. Nucl. Med. **26**(10), 1247–1250 (1999).

[23] V. Bettinardi, E. Pagani, M. Gilardi, S. Alenius, K. Thielemans, M. Teras, and F. Fazio, "Implementation and evaluation of a 3D one-step late reconstruction algorithm for 3D positron emission tomography brain studies using median root prior," Eur. J. Nucl. Med. Mol. Imaging **29**(1), 7–18 (2002).

[24] A. Reilhac, S. Tomei, I. Buvat, C. Michel, F. Keheren, and N. Costes, "Simulation-based evaluation of OSEM iterative reconstruction methods in dynamic brain PET studies," Neuroimage **39**(1), 359–368 (2008).

[25] J. Verhaeghe and A. J. Reader, "AB-OSEM reconstruction for improved Patlak kinetic parameter estimation: a simulation study," Phys Med Biol **55**(22), 6739–6757 (2010).

[26] M. J. Bélanger, J. J. Mann, and R. V. Parsey, "OS-EM and FBP reconstructions at low count rates: effect on 3D PET studies of [^{11}C] WAY-100635," Neuroimage **21**(1), 244–250 (2004).

[27] M. Conti, L. Eriksson and V. Westerwoudt, "Estimating image quality for future generations of TOF PET scanners," IEEE Trans. Nucl. Sci. **60**(1), 87–94 (2013).

[28] K. Thielemans, C. Tsoumpas, S. Mustafovic, T. Beisel, P. Aguiar, N. Dikaios, and M. W. Jacobson, "STIR: Software for Tomographic Image Reconstruction Release 2," Phys. Med.Biol. **57**(4), 867–883 (2012).

[29] A. S. Fokas, A. Iserles, and V. Marinakis, "Reconstruction algorithm for single photon emission computed tomography and its numerical implementation," J. R. Soc. Interface **3**(6), 45–54 (2006).

[30] G. A. Kastis, A. Gaitanis, Y. Fernandez, G. Kontaxakis, and A. S. Fokas, "Evaluation of a Spline Reconstruction Technique: Comparison with FBP, MLEM and OSEM," *Nuclear Science Symposium Conference Record*, IEEE (2010).

[31] P. J. La Rivière and X. Pan, "Spline-based inverse radon transform in two and three dimensions," IEEE Trans. Med. Imaging **45**(4), 2224–2231 (1998).

[32] S. Horbelt, M. Liebling, and M. Unser, "Discretization of the Radon transform and of its inverse by spline convolutions," IEEE Trans. Med. Imag. **21**(4), 363–376 (2002).

[33] A. S. Fokas and R. G. Novikov, "Discrete analogues of the $\overline{\partial}$ equation and of Radon transform," C. R. Acad. Sci. Paris **313**(2), 75–80 (1991).

[34] S. R. Cherry and M. Dahlbom, "PET: Physics, Instrumentation, and Scanners," Phelps M E ed *PET: Physics, Instrumentation, and Scanners* (Springer, New York, 2010) pp. 76.

[35] V. Bettinardi, M. Danna, A. Savi, M. Lecchi, I. Castiglioni, M. K. Gilardi, H. Bammer, G. Lucignani, and F. Fazio, "Performance evaluation of the new whole-body PET/CT scanner: Discovery ST," Eur. J. Nucl. Med. Mol. Imaging **31**(6), 867–881 (2004).

[36] L. MacDonald, J. Edwards, T. Lewellen, D. Haseley, J. Rogers, and P. Kinahan, "Clinical imaging characteristics of the positron emission mammography camera: PEM Flex Solo II," J. Nucl. Med. **50**(10), 1666–1675 (2009).

[37] M. J. Park, K. S. Park, J. S. Leek, Y. K. Kim, and D. S. Lee, "Validation of a GATE model for the simulation of a Trionix TRIAD SPECT camera," J Korean Phys. Soc. **55**(2), 681–687 (2009).

[38] E. J. Hoffman, P. D. Cutler, W. M. Digby, and J. C. Mazziotta, "3D phantom to simulate cerebral blood flow and metabolic images for PET," IEEE Trans. Nucl. Sci. **37**(2), 616–620 (1990).

[39] Y. Wang, J. Seidel, B. M. W. Tsui, J. J. Vaquero, and M. G. Pomper, "Performance evaluation of the GE Healthcare eXplore VISTA dual-ring small-animal PET scanner," J. Nucl. Med. **47**(11), 1891–1900 (2006).

[40] M. Xu, W. K. Luk, P. D. Cutler, and W. M. Digby, "Local threshold for segmented attenuation correction of PET imaging of the thorax," IEEE Trans. Nucl. Sci. **41**(4), 1532–1537 (1994).

[41] M. Defrise, P. E. Kinahan, D. W. Townsend, C. Michel, M. Sibomana, and D. F. Newport, "Exact and approximate rebinning algorithms for 3-D PET data," IEEE Trans. Med. Imag. **16**(2), 145–158 (1997).

[42] NEMA, "NEMA NU 4-2008: Performance measurements of small animal positron emission tomographs," *National Electrical Manufacturers Association*, Rosslyn, VA (2008).

[43] M. D. Abramoff, P. J. Magalhaes, and S. J. Ram, "Image processing with ImageJ," Biophotonics International **11**(7), 36–42 (2004).

[44] A. M. Loening and S. S. Gambhir, "AMIDE: A Free Software Tool for Multimodality Medical Image Analysis," Mol. Imaging **2**(3), 131–137 (2003).

[45] R. Clackdoyle, F. Noo, J. Guo, and J. A. Roberts, "A quantitative reconstruction from truncated projections in classical tomography," IEEE Trans. Nucl. Sci. **51**(5), 2570–2578 (2004).

[46] R. Clackdoyle and F. Noo, "A large class of inversion formulae for the 2D Radon transform of functions of compact support," Inverse Probl. **20**(4), 1281–1291 (2004).

[47] M. Defrise, F. Noo, R. Clackdoyle, and H. Kudo, "Truncated Hilbert transform and image reconstruction from limited tomographic data," Inverse Probl. **22**(3), 1037–1053 (2006).

[48] F. Noo, R. Clackdoyle, and J. D. Pack, "A two-step Hilbert transform method for 2D image reconstruction," Phys. Med. Biol. 49(17), 3903–3923 (2004).

[49] G. L. Zeng, "Image reconstruction via the finite Hilbert transform of the derivative of the backprojection," Med. Phys. **34**(7), 2837–2843 (2007).